Les Cahiers du GERAD ISSN: 0711–2440

On power optimization of aircraft electro-thermal anti-icing systems

M. Pourbagian, B. Talgorn,
W.G. Habashi, M. Kokkolaras,
S. Le Digabel

G–2014–72

September 2014

GERAD HEC Montréal
3000, chemin de la Côte-Sainte-Catherine
Montréal (Québec) Canada H3T 2A7

Tél. : 514 340-6053
Téléc. : 514 340-5665
info@gerad.ca
www.gerad.ca

On power optimization of aircraft electro-thermal anti-icing systems

Mahdi Pourbagian [a]

Bastien Talgorn [b]

Wagdi G. Habashi [a]

Michael Kokkolaras [b]

Sébastien Le Digabel [c]

[a] *CFD Laboratory, Department of Mechanical Engineering, McGill University, Montréal (Québec) Canada, H3A 2S6*

[b] *GERAD & Department of Mechanical Engineering, McGill University, Montréal (Québec) Canada, H3A 0C3*

[c] *GERAD & Department of Mathematics and Industrial Engineering, Polytechnique Montréal, Montréal (Québec) Canada, H3C 3A7*

mahdi.pourbagianbarzi@mail.mcgill.ca
bastien.talgorn@gerad.ca
michael.kokkolaras@mcgill.ca
sebastien.le.digabel@gerad.ca

September 2014

Les Cahiers du GERAD

G–2014–72

Abstract: Various constrained problem formulations for the optimization of an electro-thermal wing anti-icing system in both running-wet and evaporative regimes are presented. The numerical simulation of the system is performed by solving the conjugate heat transfer (CHT) problem between the fluid and solid domains. The optimization goal is to reduce the energy use and power demand of the anti-icing system while ensuring a safe protection. The formulations are carefully proposed from the physical and mathematical viewpoints; their performance is assessed by means of several numerical test cases to discern the most promising for each regime. The design optimization is conducted using the Mesh Adaptive Direct Search (MADS) algorithm using quadratic or statistical surrogate models in the search step. The influence of the models on the convergence rate and the quality of the obtained design solutions is investigated.

Key Words: Aircraft icing, electro-thermal anti-icing system, conjugate heat transfer, optimization, statistical surrogate.

Acknowledgments: This work was partially supported by a McGill Engineering Doctoral Award (MEDA), a GERAD postdoctoral fellowship and NSERC Discovery Grants 418250-2012 and 436193-2013. The authors would also like to thank the CLUMEQ consortium for its computer resources.

1 Introduction

In-flight icing is a major concern for the airworthiness and safety of commercial aircraft. It occurs when an aircraft is flying through a cloud of supercooled water droplets that are in a metastable thermodynamic equilibrium, at or below water freezing temperature. When hit by the body of the aircraft, the droplets go through a phase transition from liquid to solid. They may freeze instantaneously or run downstream and freeze later. The former occurs at lower temperatures, resulting in rime ice and the latter occurs at higher temperatures, resulting in glaze ice.

Wings and lifting components are the most sensitive parts to the threat of ice accretion because their fundamental aerodynamic characteristics, i.e. drag, lift and moments are highly affected by the ice contamination. Ice accretion increases the drag by adding to the surface roughness and decreases the maximum lift and stall angle of attack by inducing earlier boundary layer transition to turbulent flow. To avoid such detrimental effects, ice detectors, such as piezoelectric transducers, pulse echo and microwave controllers, are used to detect any ice formation on critical surfaces. Once detected, ice can be prevented (anti-icing) or removed (de-icing) by ice protection systems (IPS).

A wide range of in-flight ice protection systems have been developed and used, but in general they can be classified into three categories: liquid-based (such as weeping wings), mechanical-based (such as pneumatic boots) and thermal-based (such as hot-air and electro-thermal systems) (Thomas et al. 1996). Hot-air system consists of a circulation system, called piccolo tube, which transfers high-temperature bleed-air from the engine compressor, making a jet flow impingement on the inner skin of protected surfaces, such as wing leading edge. The bleed air then exits through holes located in the lower side of the wing or slat.

Hot-air systems have been the most widely used technology for commercial turbofan aircraft. The high amount of hot engine-core air required, from the ever-larger bypass ratio turbofans of modern aircraft, has forced the aerospace industry to move toward other alternatives. The advent of aircraft with higher generation capacity of electric power has opened the door to a more suitable technology, i.e. electro-thermal systems. In these systems, several heating pads are embedded on the inner wall of the protected leading edge. The heating pads may then be activated simultaneously for anti-icing or sequentially for de-icing protection to warm up the leading edge. These systems are considerably more efficient than the traditional hot-air systems as there is no exhausted energy. Therefore, the required power demand is almost half that of hot-air systems. Furthermore, because the electro-thermal IPS can be fully integrated into composite structures and no bleed air exhausts through holes, aircraft drag and noise are decreased relative to the hot-air IPS (Sinnett 2007).

To provide a safe protection, the no-bleed systems require generation of enough electrical power on the aircraft. There are restrictions, however, on the weight generators that can be installed on an aircraft because the Fuel consumption of an aircraft heavily depends on its weight. Moreover, due to aircraft design criteria and constraints, the size and number of the generators are also restricted. Therefore the power loads should be kept as low as possible. This highlights the necessity of minimizing the energy usage of the anti-icing system, while ensuring a safe protection. The present article is focused on this topic for electrothermal systems.

Many experimental (Al-Khalil et al. 1997; Miller et al. 1997; Wright et al. 1997) and numerical (da Silva et al. 2005; Reid et al. 2011; Yaslik 1991) studies have been conducted on modeling and simulation of electro-thermal systems. However, there are fewer works available on optimizing such systems. In one of these works (Mayer et al. 2007), a wind tunnel study of electro-thermal de-icing of wind turbine blades was done to demonstrate the relation among the wing surface temperature, the heating power, the ridge formed by liquid water runback and the meteorological conditions. Another study (Strehlow and Moser 2009) introduced a recent development in electrothermal heating technology that enables increased power densities on the leading edge of aircraft wings for the purpose of de-icing. In another work (Buschhorn et al. 2013), the application of conductive polymer nanocomposites in making highly efficient electro-thermal IPS was tested under a range of icing conditions. In (Reid et al. 2013a; Reid et al. 2013b), numerical approaches to performance degradation analysis and to provide guidelines for the design of wind turbine electro-thermal anti-icing systems, are presented. *Clean Sky*, an aeronautical research program in Europe, has recently launched a project on the combination of smart coatings with electro-thermal systems to minimize the runback ice over natural laminar flow wings' surfaces. There are also a number of studies focused on the parametric analysis (Pourbagian and Habashi 2012) and on the optimization of electro-thermal systems in anti-icing (Pourbagian and Habashi 2013b) and de-icing (Pourbagian and Habashi 2013a) modes. More recently, the authors of the present article performed a research work (Pourbagian and Habashi 2013c) on the optimization of electro-thermal anti-icing systems. In that work, to reduce the computational cost, the numerical simulations of IPS, needed at each iterate of the optimization, were replaced by reduced order models. As was shown, using these approximate models within the optimization process may result in an optimal set of design variables that is not feasible when numerically simulated. Hence in the present study, the numerical simulation of IPS using conjugate heat transfer (CHT) is directly used through the optimization process. As a complement to the previous work, the present research is focused on further development of suitable and rational constraint formulations for the optimization problem. The performance of the formulations are compared by means of numerical examples. Moreover, a surrogate optimization approach is investigated: two different statistical relevance criteria are used in the search step of the Mesh Adaptive Direct Search (MADS) optimization algorithm. The first one is based on a chance constraint and the second is based on the expected improvement. The effects of these models on the performance of the optimization process are also investigated.

2 CHT simulation of electro-thermal IPS

An overall schematic of the optimization process is shown in Fig. 1. The CHT simulation of the IPS is performed for the given flight-icing conditions. The solution is then used to evaluate the objective function and constraints while the optimization algorithm is used to determine the value of the design variables iteratively until convergence is achieved relative to some defined criteria.

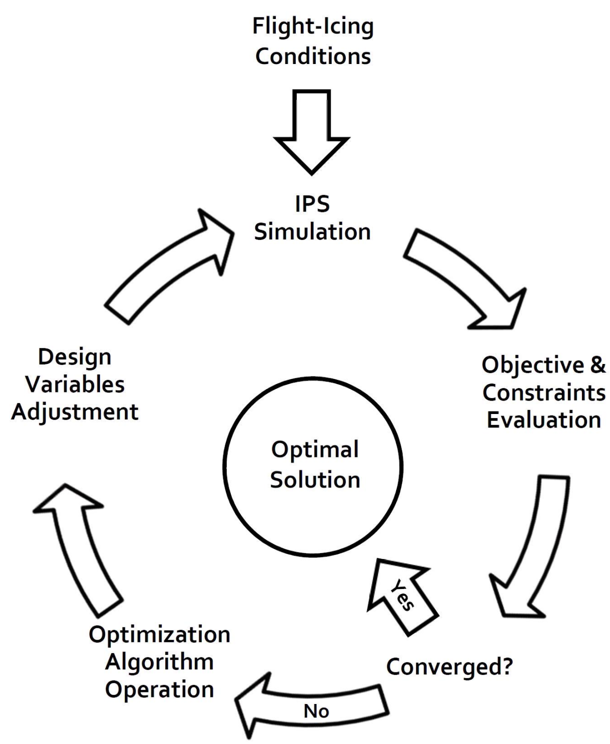

Figure 1: Schematic of the optimization process

As a requirement for the IPS, the simulation of in-flight icing is considered first, which is a multi-step procedure consisting of solving for the airflow, droplet impingement and ice accretion. The overall framework of icing simulation is illustrated in Fig. 2. After obtaining the airflow solution, the velocity field is used to compute the droplet impingement. Then, friction forces and heat fluxes from the airflow solution along with the droplet velocity field from the droplet impingement solution are used to compute the surface node

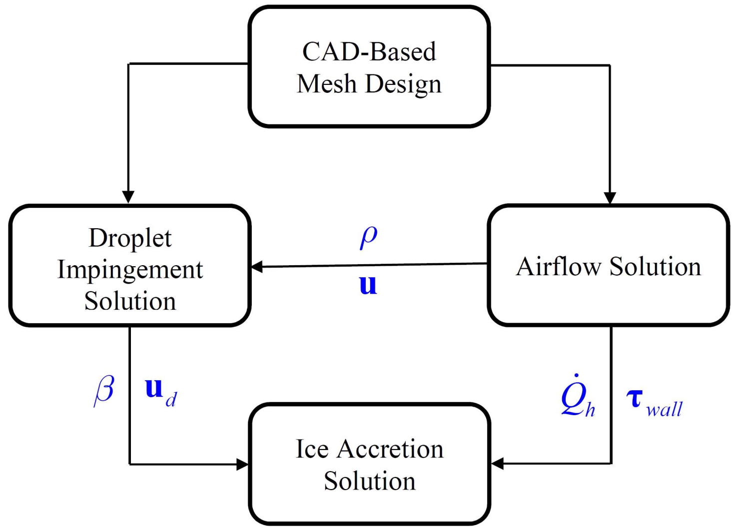

Figure 2: Overall framework of in-flight icing simulation

displacement due to ice accretion. In this work, the in-house high-fidelity FENSAP-ICE system (Beaugendre et al. 2006) consisting of a collection of modules (FENSAP, DROP3D, ICE3D), is used to solve different disciplines. In this system, the viscous turbulent airflow solution is obtained via a Reynolds-Averaged Navier-Stokes (RANS) approach, and using the Spalart-Allmaras one-equation turbulence model. The droplet impingement is also calculated by means of an Eulerian approach. For the ice accretion, the Messinger-based (Messinger 1953) thermodynamic balance is performed by applying partial differential equations of mass and energy balances (Equations (1) and (2)) for the water film on the surface as follows: the mass balance equation includes droplet impingement as the source, and evaporation and ice accretion as the sinks, and the energy balance consists of the heat transferred by droplet impingement, evaporation, ice accretion, convection, radiation, in addition to the heat conduction through the metal skin of the wing (the tilde denotes temperature measured in °C):

$$\rho_w \left[\frac{\partial h_f}{\partial t} + \nabla \cdot (\overline{\mathbf{u}}_f h_f)\right] = U_\infty \mathrm{LWC}\beta - \dot{m}''_{evap} - \dot{m}''_{ice}, \tag{1}$$

$$\begin{aligned}\rho_w \left[\frac{\partial h_f c_w \widetilde{T}}{\partial t} + \nabla \cdot \left(\overline{\mathbf{u}}_f h_f c_w \widetilde{T}\right)\right] = &\left[c_w \widetilde{T}_{d,\infty} + \frac{\|u_d\|^2}{2}\right] U_\infty \mathrm{LWC}\beta \\ &- 0.5\left(L_{evap} + L_{subl}\right)\dot{m}''_{evap} + \left(L_{fusion} - c_{ice}\widetilde{T}\right)\dot{m}''_{ice} + h_c\left(T_\infty - T\right) \\ &+ \varepsilon\sigma\left(T_\infty^4 - T^4\right) + \dot{Q}''_{IPS},\end{aligned} \tag{2}$$

where ρ_w being the water density, h_f the water film height, $\overline{\mathbf{u}}_f$ the water film velocity vector, U_∞ and u_d the velocity of freestream and water droplet, respectively, LWC the liquid water content of the airflow, β the collection efficiency, $\dot{m}''_{evap}$ and $\dot{m}''_{ice}$ the mass flux of evaporation and ice accretion, respectively, c_w and c_{ice} the specific heat capacity of water and ice, respectively, T and T_∞ the temperature at the surface and freestream, respectively, $T_{d,\infty}$ the temperature of water droplet at freestream, L_{evap}, L_{subl} and L_{fusion} the latent heat of evaporation, sublimation and fusion, respectively, h_c the convective heat transfer coefficient, ε the emissivity coefficient, σ the Stefan-Boltzmann constant and $\dot{Q}''_{IPS}$ the heat flux provided by the ice protection system.

Once calculated, the ice accretion solution is used in conjunction with the heat conduction solution of the wing's composite shell by solving the conjugate heat transfer problem between the fluid and the solid using the CHT3D (Croce et al. 2002) module of FENSAP-ICE. This is performed by making the various disciplines converge using a fixed-point iteration process that exchanges the thermal boundary conditions among the external airflow, water film and solid skin (Fig. 3). It should be noted that a constant heat transfer coefficient is used to reduce the computational cost. This coefficient, which is obtained from the solution of the Navier-Stokes equations at the beginning of the CHT process, is used throughout the CHT iterations to avoid repeating solving the expensive Navier-Stokes equations (Pourbagian and Habashi 2013c).

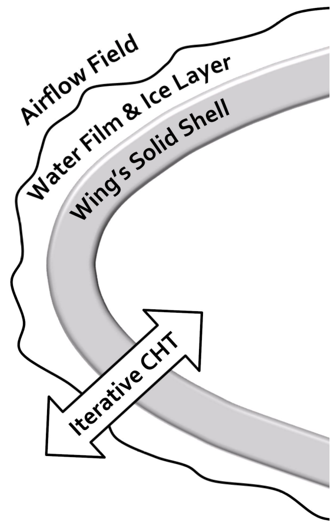

Figure 3: Three domains involved in the CHT procedure

3 Problem statement

3.1 General description

A general statement of the considered optimization problem can be given as:

$$\begin{aligned} \min_{x \in \chi} \quad & f(x) \\ \text{subject to} \quad & c_j(x) \leq 0, \quad j \in J, \end{aligned} \tag{3}$$

where f is the objective function, x is the vector of n design variables, c_j's are the constraints, $J = \{1, 2, \cdots, m\}$ and χ is a subset of $\mathbb{R}^n$. The electro-thermal IPS is a NACA 0012 model used in the experimental tests performed in the NASA Lewis Icing Research Tunnel (Al-Khalil et al. 1997). As shown in Fig. 4, seven electric heating blankets are embedded inside a four-layer composite panel including erosion shield, elastomer, fiberglass, and silicone foam. The design variables, which include the power densities (in W/m^2) of the seven heating blankets, are defined in [1,000; 15,000] for the running-wet regime cases, and in [1,000; 30,000] for the evaporative regime cases. The objective function and constraints, as mentioned, are obtained by the CHT simulation that is considered as a blackbox. The objective function, f, is the total electric power used for anti-icing:

$$f(\mathbf{x}) = \int_{s_{el}}^{s_{eu}} P''(s)\, ds, \tag{4}$$

where s is the wrap (surface) distance measured from the leading edge, which is negative on the lower and positive on the upper surface, and $P''(s)$ is the power density at the position s. The domain of integration is the interval between the wrap distance of the end of the protected zone on the lower surface, s_{el}, and that on the upper surface of the wing, s_{eu}.

3.2 Constraint formulations

Table 1 provides the various constraint formulations that are proposed in this work. *MIG* stands for "maximum ice growth" over the heating zone. It should be noted that the ice growth is computed as a distribution over the wing surface and its maximum value is considered as the constraint. As an alternative to the ice

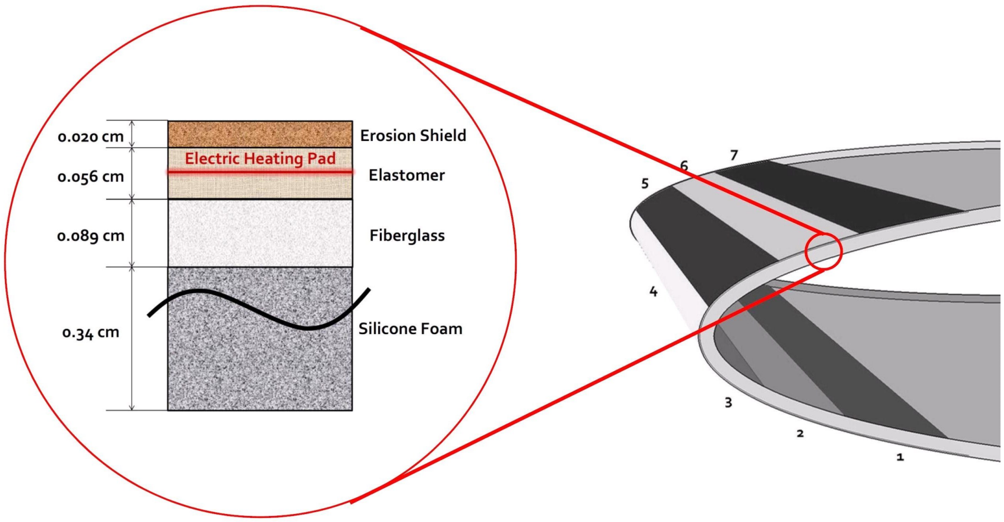

Figure 4: Schematic picture of the electro-thermal IPS

Table 1: Various formulations of the constraint

Type	Formulation	Description
MIG	$\max\left\{\dot{m''}_{ice}(s)\right\}_{s_{el}}^{s_{eu}}$	Maximum ice growth
MWT	$T_0 - \min\{T(s)\}_{s_{el}}^{s_{eu}}$	Minimum wall temperature
TWT	$\int_{s_{el}}^{s_{eu}} \lvert T_t(s) - T(s)\rvert\, ds$	Target wall temperature
$(TMWT)_d$	$\int_{s_{el}}^{s_{eu}} \tau_d(T)\, ds$	Target-minimum wall temperature-discontinuous
$(TMWT)_c$	$\int_{s_{el}}^{s_{eu}} \tau_c(T)\, ds$	Target-minimum wall temperature-continuous
EFH	$h_f(s_{el}) + h_f(s_{eu})$	End film height
$(DEFH)_{lo}$	$\eta\left(h_f(s_{el})\right)$	Distance-end film height on the lower surface
$(DEFH)_{up}$	$\eta\left(h_f(s_{eu})\right)$	Distance-end film height on the upper surface
MST	$\max\{T_{shell}\} - T_*$	Maximum composite shell temperature

growth, the (skin) wall temperature may be used. This is to be considered in different forms: MWT, standing for "minimum wall temperature", poses the limit T_0 on minimum temperature of the wall over the heating surface, while TWT, standing for "target wall temperature", sets the target T_t for the temperature distribution. $(TMWT)_d$ (subscript d refers to "discontinuous") also poses a limit on minimum temperature of the wall, but it is based on the following function definition:

$$\tau_d(T) = \begin{cases} (T_0 - T) & \text{if } \min\{T(s)\}_{s_{el}}^{s_{eu}} \geq T_0, \\ \max\{0, (T_0 - T)\} & \text{if } \min\{T(s)\}_{s_{el}}^{s_{eu}} < T_0. \end{cases} \tag{5}$$

The above equation separates the definition of the feasible regions, i.e. $\min\{T(s)\}_{s_{el}}^{s_{eu}} \geq T_0$, from that of the infeasible regions, i.e. $\min\{T(s)\}_{s_{el}}^{s_{eu}} < T_0$. Fig. 5 illustrates a schematic of $\tau_d(T)$. The reason of using such definition, and not simply using $(T_0 - T)$ for all ranges of $\min\{T(s)\}_{s_{el}}^{s_{eu}}$, is that the integral of the feasible regions may outbalance that of the infeasible regions, resulting in a net feasible output even if there are some regions with infeasible temperature (Fig. 6). It is noticed that for marginal cases where

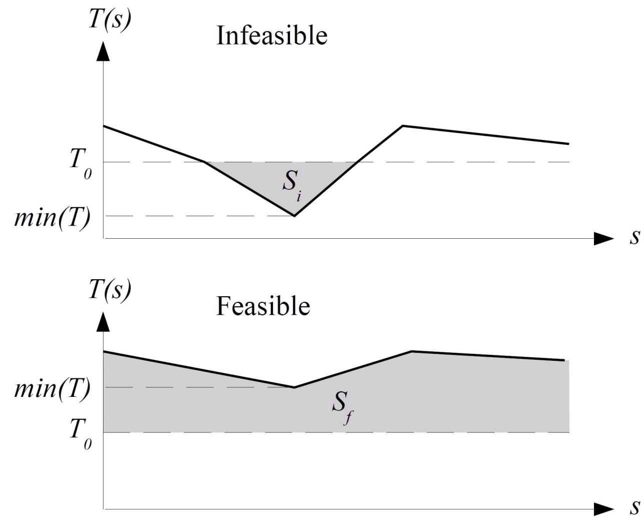

Figure 5: Illustration of the constraint $TMWT$ for infeasible and feasible cases (S_i is the surface integration of temperature profile over infeasible parts and S_f is that over feasible parts)

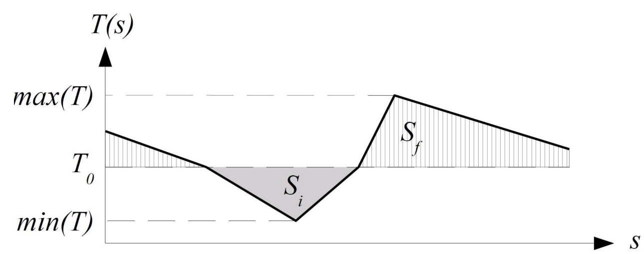

Figure 6: An infeasible case with net feasible output (S_i is the surface integration of temperature profile over infeasible parts and S_f is that over feasible parts)

$\min\{T(s)\}_{s_{el}}^{s_{eu}}$ is very close to T_0, if $\min\{T(s)\}_{s_{el}}^{s_{eu}}$ slightly varies, a discontinue jump in the function value occurs. This may be circumvented by defining *(TMWT)$_c$* (subscript c refers to "continuous") that uses the following function, where the second condition is the same as that of $\tau_d(T)$ but the first one is changed to a point value:

$$\tau_c(T) = \begin{cases} \min\{T(s)\}_{s_{el}}^{s_{eu}} & \text{if } \min\{T(s)\}_{s_{el}}^{s_{eu}} \geq T_0, \\ \max\{0, (T_0 - T)\} & \text{if } \min\{T(s)\}_{s_{el}}^{s_{eu}} < T_0. \end{cases} \tag{6}$$

The next constraint, introduced in Table 1, is *EFH* that stands for "end film height". It is equal to the summation of the water film height at the end of the protected zone on the upper and lower surfaces of the wing. This quantity is important since to avoid formation of ice after the protected zone, water shall not pass beyond the zone. *EFH* is a non-negative value and this affects the searchability of the design space for feasible solutions. According to Fig. 7, a good constraint formulation would be a quantifiable constraint, i.e. one that provides a distance to infeasibility as well as a distance to feasibility.

Therefore, as an alternative to *EFH*, a "distance-to-end film height", i.e. *(DEFH)lo* and *(DEFH)up*, may be defined (*lo* and *up* refer to lower and upper surfaces, respectively) using the following function definition:

$$\eta(h_f(s_e)) = \begin{cases} h_f(s_e) & \text{if } h_f(s_e) > 0, \\ -d_f(s_e) & \text{if } h_f(s_e) = 0, \end{cases} \tag{7}$$

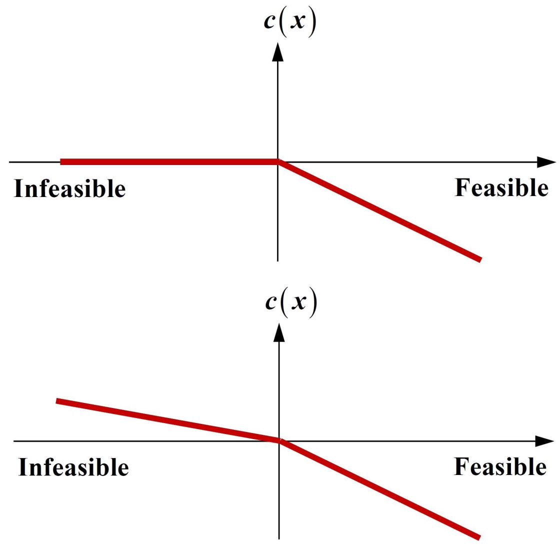

Figure 7: Bad (top) and good (bottom) constraint formulations

where $h_f(s_e)$ is the water film height at the end of the heating zone on the upper or lower surfaces, and $d_f(s_e)$ is the distance between the point at which the water film is completely evaporated and the end of the heating zone on the upper or lower surfaces (Fig. 8).

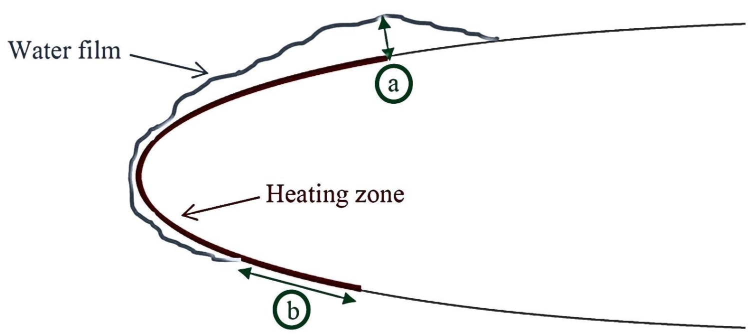

Figure 8: Illustration of the constraint *DEFH* for positive (a) and negative (b) values

The mechanical properties of aircraft structure are highly dependent on temperature. The ultimate strength, the yield strength and the fatigue life of many composite materials decrease as temperature increases (Mivehchi and Varvani-Farahani 2010). Moisture is also more corrosive at higher temperatures because of the normal increase in reaction rate and the larger hydrogen ion activity due to lower pH (Hackerman 1952). This becomes more critical when considering *thermal spiking*, which describes the effect of a rapid increase in temperature of a composite with high moisture content (Baker et al. 2004). It can damage the matrix, giving rise to moisture absorption into the composite and limiting the maximum temperature at which a composite can operate. Finally, large temperature differences cause non-uniform expansions in different parts of the structure, resulting in higher thermal stresses, added to the other imposed stresses (Starke 1996). In light of the abovementioned motives, it seems essential to restrict the maximum temperature of the composite shell, inside which the electro-thermal IPS is embedded. *MST*, standing for "maximum shell temperature", as provided in Table 1, poses such limit, i.e. T_*. It should be noted that the maximum temperature takes place inside the shell and not on the external wall, as the heating blankets are placed inside the shell.

4 Optimization method

The optimization problem defined in Equation (1) is solved by the MADS algorithm (Audet and Dennis 2006). MADS is a derivative-free method based on a *search-and-poll* paradigm. The search is a flexible and optional method that allows to take into account the specificities of the problem and the insights of the user. It can consist of any exploration method, like genetic algorithms (Goldberg 1989), particle swarms (Vaz and Vicente 2007), Latin hypercube (McKay et al. 2000) or variable neighborhood search (Audet et al. 2008). In this work, the search is a surrogate-based search that uses the dynaTree library (Taddy et al. 2011) to build predictive models of the objective and the constraints. The poll is the rigorous step of MADS on which the convergence relies.

4.1 The poll step

At each iteration k of the MADS algorithm, the *mesh* is defined as:

$$M_k = \{x + \Delta_k^m D z : z \in \mathbb{N}^{n_D}, x \in \mathbf{X}_k\} \subset \mathbb{R}^n, \tag{8}$$

where $\mathbf{X}_k = \{x_1, x_2, \ldots\} \in \mathbb{R}^n$ is the set of all the points previously evaluated, Δ_k^m is the *mesh size parameter* at iteration k, and the directions of D are positively spanning $\mathbb{R}^n$. To ensure convergence, all candidates evaluated at iteration k must lie on M_k. The set of trial points is $P_k = \{x_k + \Delta_k^p d : d \in D_k\}$, where the poll directions D_k are combinations of the directions of D whose norm is at most Δ_k^p , the *poll size parameter* that bounds the distance between the trial points and x_k. Fig. 9 illustrates the progressive diminution of the mesh size and the poll size parameters. MADS controls the mesh size to belittle faster than the poll size, implying the possible set of polling directions to grow dense in the unit sphere, once normalized. The MADS algorithm ensures global convergence (i.e. independent of the starting point x_0) toward a local optimum satisfying local optimality conditions based on the Clarke calculus for nonsmooth functions (Clarke 1983).

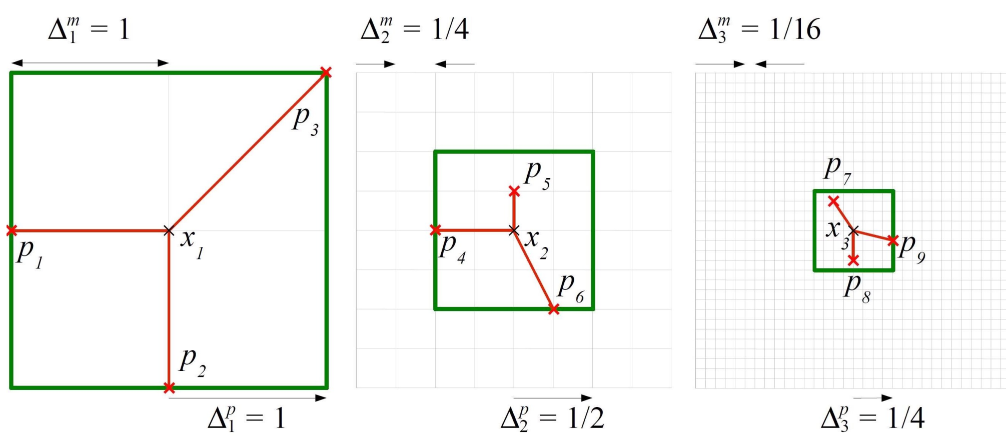

Figure 9: Mesh and poll size parameters

4.2 The dynaTree library

The dynaTree package (Taddy et al. 2011) is a statistical regression method. From $\mathbf{X}_k$ and $y(\mathbf{X}_k)$, dynaTree builds a model of the function y by building several partitioning schemes of $\mathbb{R}^n$ and performing a linear regression in each part. Thus, the prediction on y is piecewise linear. The Bayesian framework allows parameter-free regression and quantification of the deviation of the data from the model. Thus, predictions of the variance of y are available and it is also possible to compute the cumulative density function $\mathbb{P}[y(x) \leq y_0], \forall x \in \mathbb{R}^n, y_0 \in \mathbb{R}$. These predictions are used in the search step of MADS to build statistical relevance criteria of candidates. The interested reader can refer to (Taddy et al. 2011) for more details about dynaTree. In this work, the predictive mean and standard deviation of the objective in x are denoted by $\hat{f}(x)$ and $\hat{\sigma}_f(x)$. Similarly, for the constraint c_j, they are denoted by $\hat{c}_j(x)$ and $\hat{\sigma}_j(x)$, $j \in J$.

4.3 Statistical relevance

The *expected improvement* (Jones 2001; Jones et al. 1998) is a statistical relevance criteria introduced for global optimization. Let $f_{\min}$ be the objective value of the best feasible point found so far. The *improvement* is defined as $\mathrm{I}(x) = \max\{f_{\min} - f(x)\,; 0\}$. Though the improvement can only be known by evaluating x, the *expected improvement* can be analytically approximated by dynaTree (Taddy et al. 2011):

$$EI(x) = \mathbb{E}[I(x)] = \int_0^{+\infty} I \phi_f(f_{\min} - I)\, dI, \tag{9}$$

where ϕ_f is the probability density function of f. Fig. 10 shows an example of dynaTree model for 24 data points $\mathbf{X} = \{x_1, \ldots, x_{24}\} \subset [0;\, 25]$. The first part of the diagram shows the decision tree that allows to find out in which leaf $\eta \in \{\eta_1, \ldots, \eta_6\}$ lies a point x. The second part of the diagram illustrates the partitioning of the interval $[0;\, 25]$. A linear regression is built in each of these parts. As we can see, the standard deviation of the model is larger in the ill explored areas. The third part of the diagram shows the probability of improvement $\mathbb{P}[y(x) < y_{min}]$, where $y_{min} = \min_{x \in X} y(x)$, and the expected improvement $EI(x), \forall x \in [0;\, 25]$.

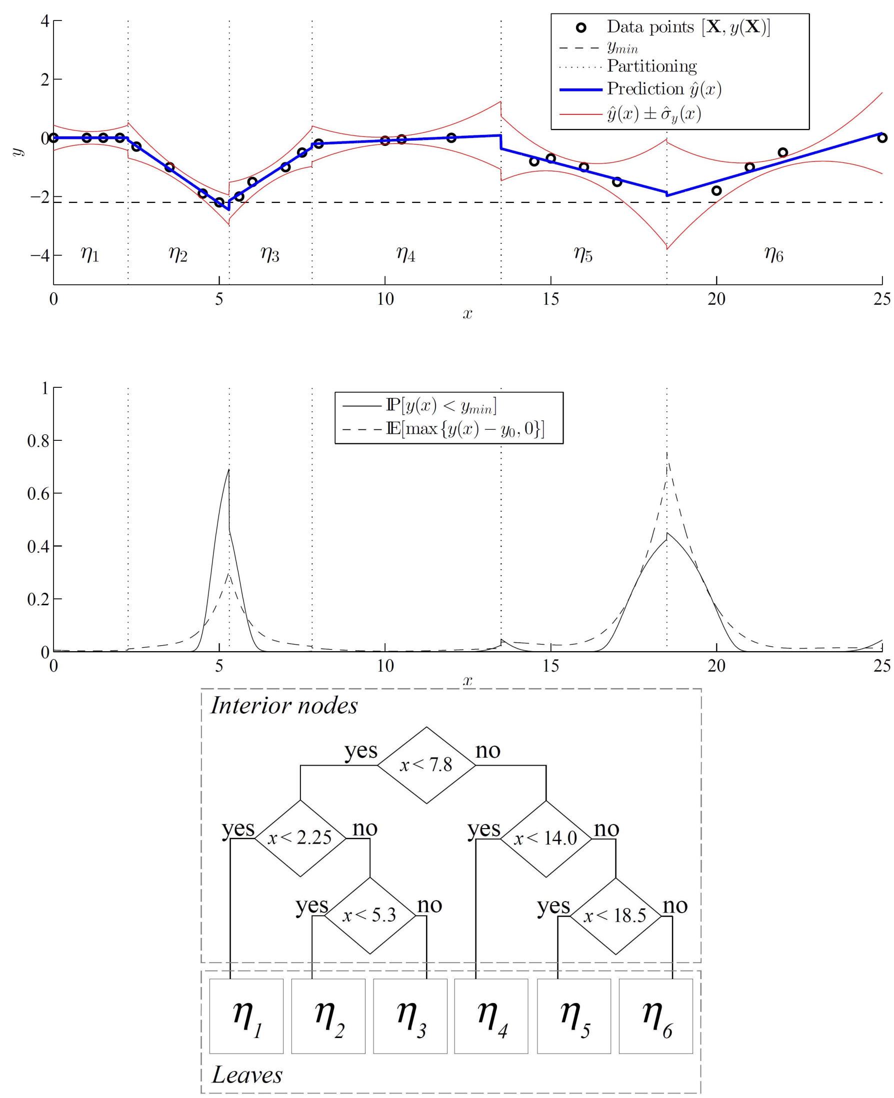

Figure 10: dynaTree model on 24 data points in $\mathbb{R}$ (picture adapted from (Talgorn et al. 2014))

The probability of improvement is maximal for $x = 5$, while the expected improvement peaks at $x = 17$. This illustrates that while the function y is very likely to have a local optimum around $x = 5$, there is a promising probability of a better optimum around $x = 17$. As dynaTree provides an approximation of the cumulative density functions of the constraints, the probability of feasibility of a point can be estimated as

$$P(x) = \prod_{j \in J} \mathbb{P}\left[c_j(x) \leq 0\right]. \tag{10}$$

This can be computed as dynaTree returns $P\left[c_j(x) \leq 0\right], \forall j \in J$. This allows to statistically describe the feasibility by one scalar value. By merging the expected improvement and the probability of feasibility, the *expected feasible improvement* is naturally defined as (Schonlau et al. 1997; Talgorn et al. 2014)

$$EFI(x) = EI(x)\, P(x). \tag{11}$$

$EFI(x)$ describes the expected income of x regarding to the optimization problem.

4.4 Lack of information

To improve the surrogate-based search, the candidates must not only be promising solutions to the optimization problem, but to some extent, they must also participate to improve the models of f and c_j, $j \in J$. In this regard, uncertainty of model predictability due to lack of information (areas of the design space where no simulations have been conducted) must be quantified, in order to favour the candidates in the ill-explored area of χ. Uncertainties about the objective can be quantified by the approximated standard deviation $\hat{\sigma}_f$ returned by dynaTree (Taddy et al. 2011). For the constraints however, uncertainty about $c_j(x), \forall j \in J$ is less important than the uncertainty on the feasibility of the point x. For example, the value of $c_1(x)$ is of little interest if c_2 is known to be not satisfied in x. Finally, the uncertainties on the feasibility can be quantified by considering that the event "x is feasible" as a Bernoulli law of parameter $P(x)$. Thus, the variance of this law is $P(x)(1 - P(x))$. We define the *uncertainty in the feasibility* (μ) (Talgorn et al. 2014):

$$\mu(x) = 4P(x)(1 - P(x)). \tag{12}$$

The coefficient 4 normalizes μ in [0; 1]. Fig. 11 shows an example of $P(x)$ and $\mu(x)$ on a single constraint c. The model of c is built from 30 evaluations in [0; 10]. The feasibility threshold is represented by the horizontal dashed line $c = 0$ and the feasible domain is approximately [4; 7]. The uncertainty μ is maximal for $x = 4$, where $c = 0$. However, the sharp variation of c at $x = 7$ does not induce a high value of μ as the feasibility prediction is adamant.

4.5 Surrogate-based search

The two surrogate-based searches considered in this work are the methods FSP and $EFIC$ described in (Talgorn et al. 2014). The FSP formulation consists of minimizing the model of the objective under the *chance constraint* $P(x) \geq 1/2$. To improve this search, exploration term based on the standard deviation of the models are added (Taddy et al. 2011). The standard deviation of the objective is considered favourably as it can lead to an improvement of the solution. The exploration term is weighted by a coefficient $\lambda \in [0; 1]$, leading to the following formulation:

$$\begin{aligned} \min_{x \in \chi} \quad & \hat{f}(x) + \lambda \hat{\sigma}_f(x), \\ \text{subject to} \quad & P(x) \geq \frac{1}{2}. \end{aligned} \tag{13}$$

The constraint $P(x) \geq 1/2$ ensures that, through the whole optimization process, half of the candidates returned by the search should be feasible. Moreover, this search will favor the exploration of the frontier of the feasible domain, where $P(x) = 1/2$. The λ parameter permits adjusting the magnitude of the exploration. While $\lambda = 0.01$ is considered as light, $\lambda = 1$ implies an intense exploration (Taddy et al. 2011).

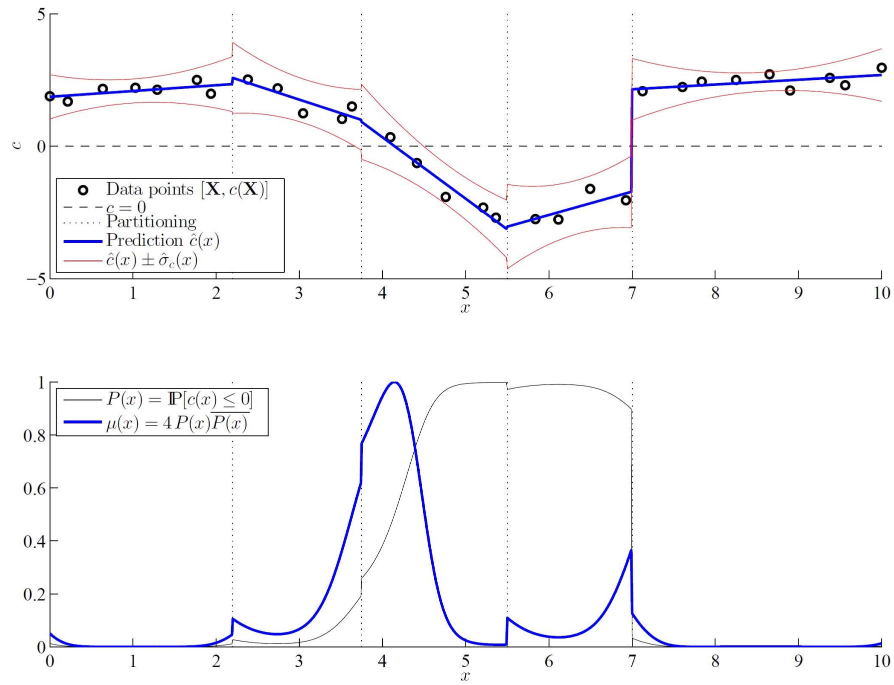

Figure 11: Probability of feasibility and uncertainty about feasibility (picture adapted from (Talgorn et al. 2014))

The $EFIC$ formulation consists of an unconstrained optimization problem based on the expected feasible improvement. EFI does not take into account the information brought by x to the models of f and c_j, $j \in J$. Thus, an exploration term $EI\,(x)\,\mu\,(x)+P\,(x)\,\hat{\sigma}_f\,(x)$ is added. The term $EI\,(x)\,\mu\,(x)$ aims to favor the points with a promising objective but with an uncertain feasibility. This term will improve the representation of the frontier of the feasible domain, where $\mu\,(x)$ is maximal. Conversely, the term $P\,(x)\,\hat{\sigma}_f\,(x)$ favours feasible points with an uncertain objective, leading to an improvement of the model of f in the feasible domain. This lead to the following formulation:

$$\max_{x \in \mathcal{X}} \quad EFI\,(x) + \lambda\,(EI\,(x)\,\mu\,(x) + P\,(x)\,\hat{\sigma}_f\,(x)) \tag{14}$$

5 Numerical test cases

The proposed constraint formulations are used to define suitable optimization problem statements. The matrix of the test cases is provided in Table 2, which includes three cases for the running-wet regime and seven cases for the evaporative regime. In this table, the constraint(s) used for each test case are identified. The optimization results were obtained using the MADS implementation from the NOMAD package (Le Digabel 2011) and the R dynaTree library (Gramacy and Taddy 2010). In the dynaTree-based optimization cases, $\lambda = 0.1$ is used as the exploration parameter. Also, the number of design variables times 100 is taken for the number of blackbox evaluations needed for each optimization problem.

A hybrid grid (Dussin et al. 2009) is used around the NACA 0012 airfoil and a structured one inside the leading edge's composite shell (Fig. 12). In the experiments (Al-Khalil et al. 1997), the heating blankets were slightly shifted toward the upper surface. This asymmetric arrangement is taken into account here in order for the comparison to be meaningful. It should be noted that the total electric power values presented are those needed per meter of the wing span. The flight-icing conditions considered for the test cases are provided in Table 3, where AoA is the angle of attack, LWC is the liquid water content and MVD is the median volumetric diameter of the droplets.

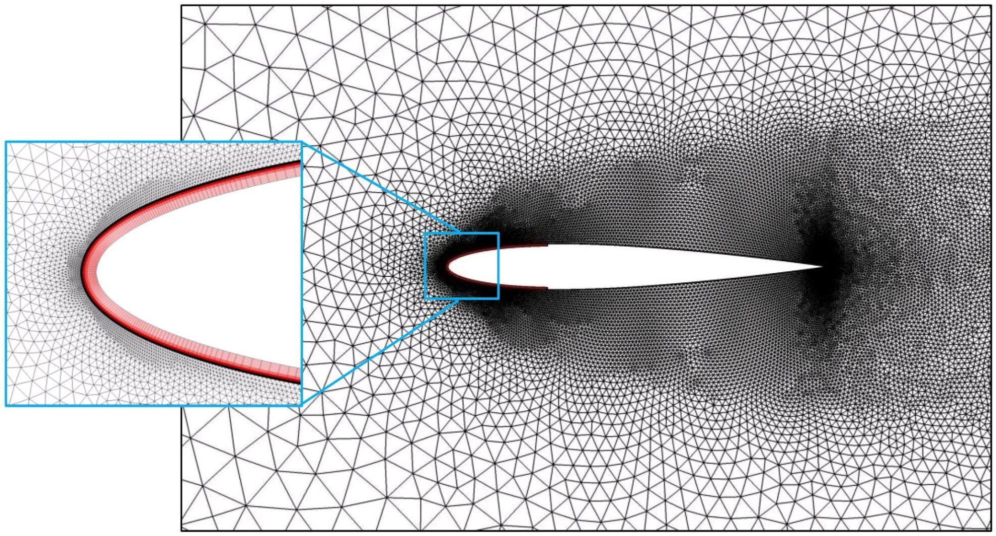

Figure 12: Hybrid grid around the NACA 0012 airfoil and structured grid inside the leading edge composite shell

Table 2: Matrix of test cases

	MIG	MWT	TWT	$(TMWT)_d$	$(TMWT)_c$	EFH	$(DEFH)_{lo}$	$(DEFH)_{up}$	MST
W-I	✓								
W-II		✓							
W-III			✓						
E-I	✓					✓			✓
E-II		✓				✓			✓
E-III				✓		✓			✓
E-IV					✓	✓			✓
E-V		✓					✓	✓	✓
E-VI				✓			✓	✓	✓
E-VII					✓		✓	✓	✓

Table 3: Flight-icing conditions

$T_\infty\,[K]$	$U_\infty\,[m/s]$	$LWC\,[g/m^3]$	$MVD\,[\mu m]$	AoA [degrees]
254.375	44.704	0.78	20	-4

5.1 Running-wet regime

Anti-icing systems may operate in either the running-wet or evaporative regimes. In the running-wet regime, the goal is to keep the protected zone free of ice. But water droplets passing beyond the protected zone may freeze, resulting in runback ice. Because of its low power requirement, the running wet regime seems to be preferable for operation of anti-icing systems. However, the risk of runback ice formation over critical downstream zones should not be ignored. Based on the general form stated in Equation (3) and the objective function in Equation (4), various constrained problem statements may be defined using the different constraints provided in Table 1. The following constraint is considered for the first case, i.e. Case W-I:

$$c_1(x) \equiv MIG. \tag{15}$$

It is recalled that MIG is the maximum ice growth over the protected zone. Fig. 13 shows the convergence history of the best feasible objective values, i.e. the objective values when $c(\mathbf{x}) \leq 0$ (actually the ice growth is a non-negative value, so feasible solutions satisfy $c(\mathbf{x}) = 0$). The optimized total electric power is 1,051 W, which is about 12% less than the value used in the experimental test (Run #91, TTMS #123), i.e. 1,199 W (Al-Khalil et al. 1997). Fig. 14 depicts the variation history of the best feasible design variables values throughout the optimization process, and Fig. 15 compares the optimized and experimental power densities. The heaters on the lower surface, i.e. heaters 1, 2 and 3, require more power density compared to the ones on the upper surface, i.e. heaters 5, 6 and 7. This is due to the negative angle of attack that results in a larger heat transfer on the lower surface because of lower pressure and higher velocity (Fig. 16).

The previous case (Case W-I) does not seem to be conservative enough as no margin of safety can be considered in such formulation. To account for that, the following constraint on the minimum wall

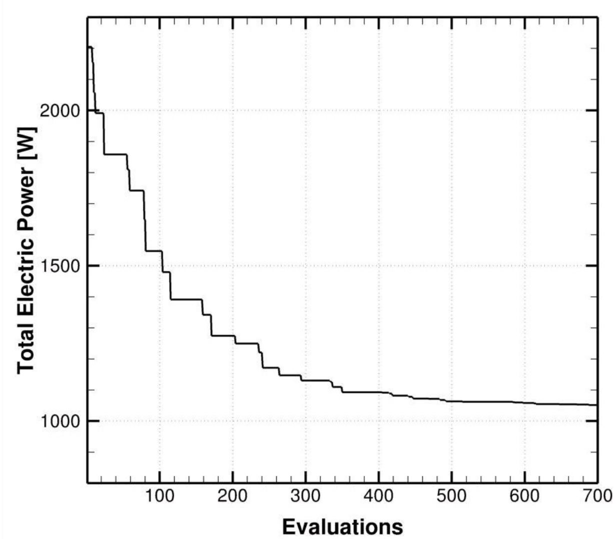

Figure 13: History of the best feasible objective values (Case W-I)

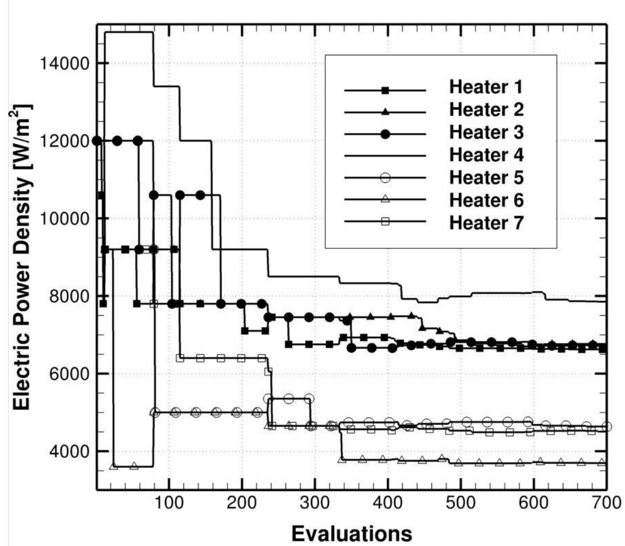

Figure 14: History of the best feasible design variables values (Case W-I)

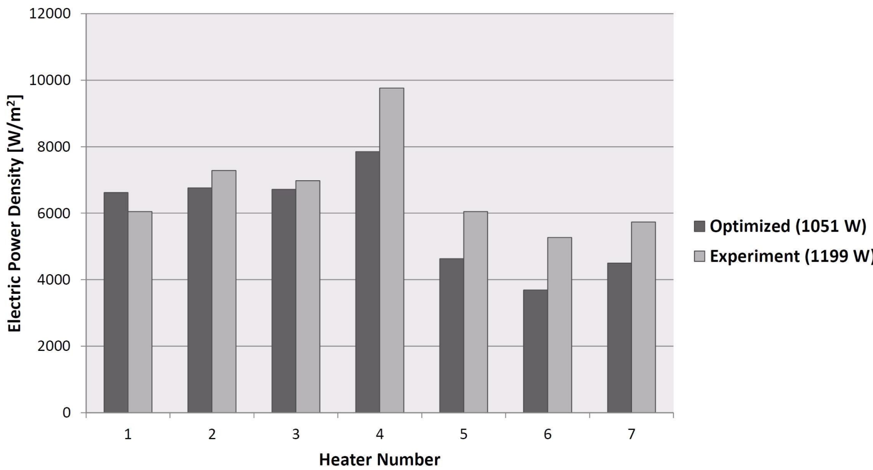

Figure 15: Optimized and experimental power densities (Case W-I)

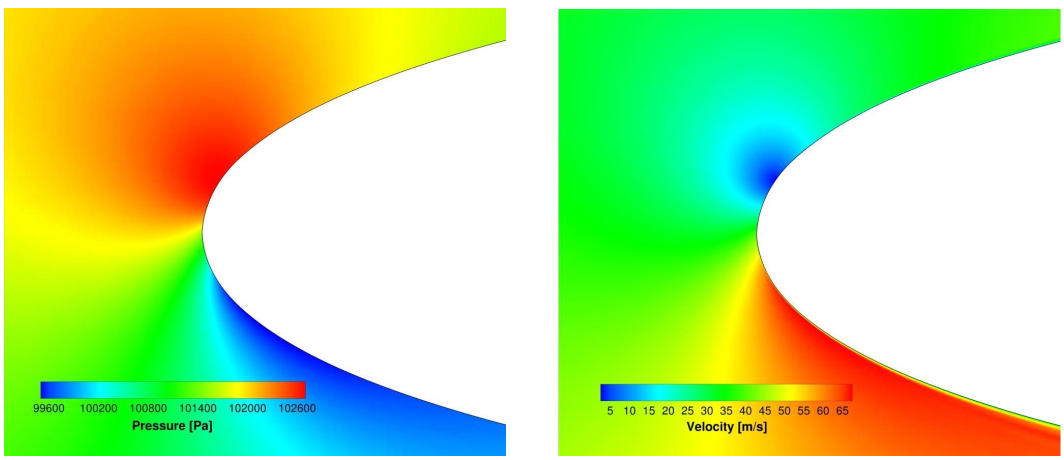

Figure 16: Pressure (left) and velocity (right) contour plots

temperature may be used for Case W-II:

$$c_1(\mathbf{x}) \equiv MWT. \tag{16}$$

By assuming $T_0 = 276\,K$, a margin is considered with respect to the freezing temperature, i.e. $273.15\,K$. In order for MWT to be efficient, the margin should not be too large, otherwise it would require excessive power usage. The minimum total electric power reached in this case is $1,386\,W$ (Fig. 17) which, because of the margin, is 32% larger than that of Case W-I, i.e. $1,051\,W$.

Another alternative being more suitable for running-wet regime is a target wall temperature, as follows (Case W-III):

$$c_1(\mathbf{x}) \equiv TWT, \tag{17}$$

where $T_\mathrm{t} = 276\,K$ is used as the target temperature. This constraint can be more efficient in terms of power usage as it ensures that the surface temperature all over the heating zone is not higher that what is actually needed. Based on the definition of TWT, provided in Table 1, this constraint does not yield a feasible solution. Hence, the objective function history is plotted based on the best constraint values (Fig. 18). The total electric power is reached to $1,172\,W$, which is 15% less than that obtained in Case W-II. Fig. 19 compares the optimized power densities between the two cases. As shown, the power density of all heating pads for Case W-III is less than that for Case W-II.

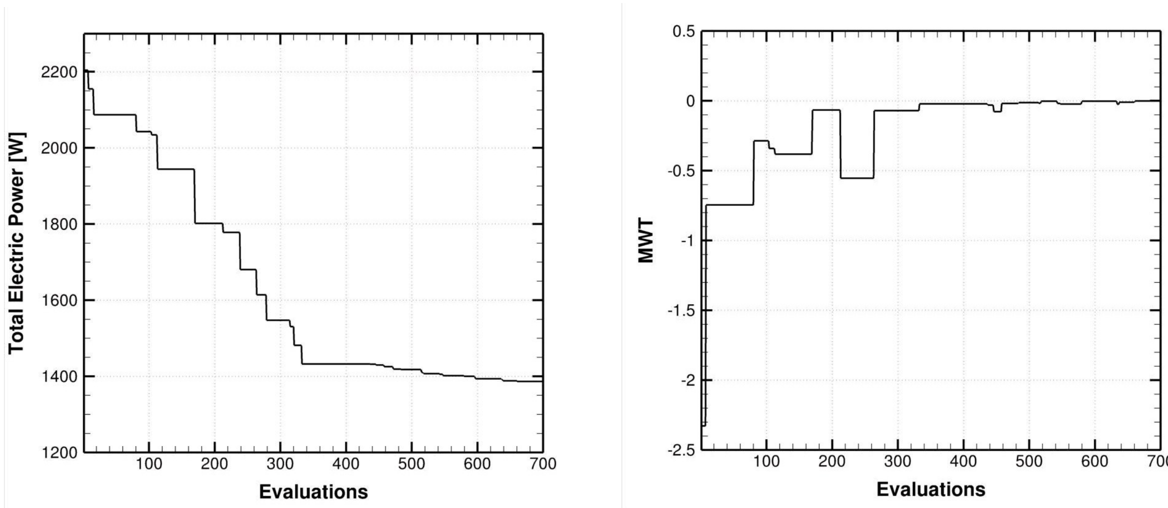

Figure 17: History of the best feasible objective (left) and constraint violation (right) values (Case W-II)

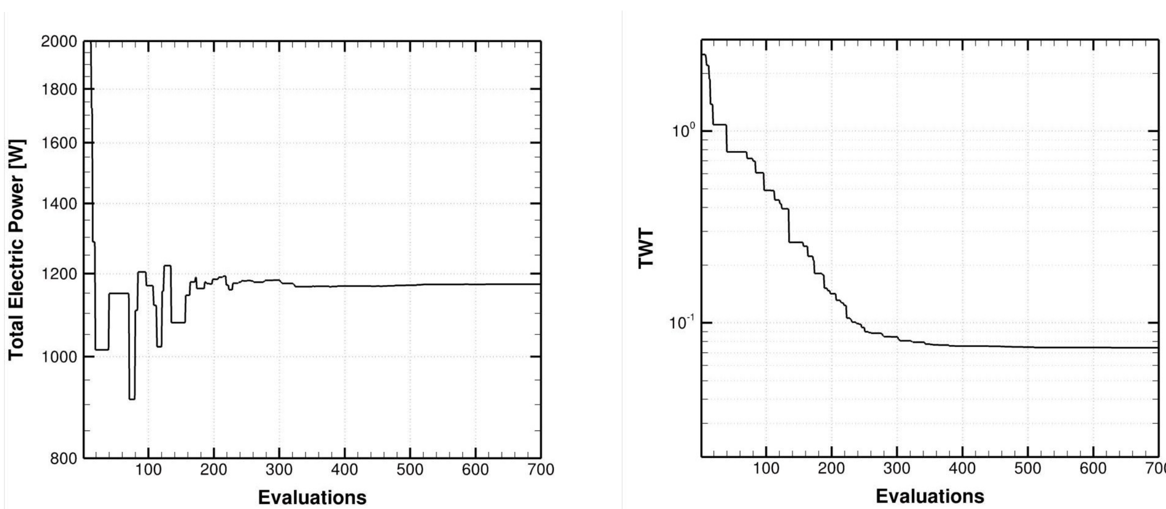

Figure 18: History of the objective values (left) based on the best constraint violation values (right) (Case W-III)

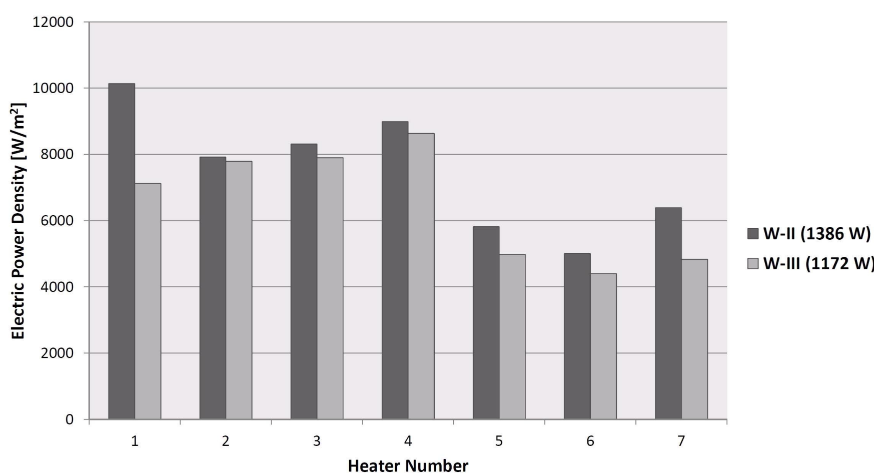

Figure 19: Optimized power densities (Case W-II and Case W-III)

In order to better compare the performance of the running-wet test cases, i.e. W-I, W-II and W-III, the profiles of three surface quantities at their optimal states are compared in Fig. 20. The wrap distance in these plots is the surface distance from the leading edge being positive on the upper surface and negative on the lower surface. As expected for the running-wet regime, runback ice is observed in all test cases because the water film passes beyond the protected zone. However, the largest amount of ice on upper and lower surfaces accretes in Case W-I. The temperature profile of Case W-III shows that the optimal state closely captures the target temperature, i.e. $T_{\rm t} = 276\,K$. It is also interesting to note that the temperature profile of Case W-I is very similar to that of Case W-III with a vertical shift toward the freezing temperature.

The test cases presented so far has been optimized using MADS without statistical surrogates. To demonstrate the influence of these surrogates on the optimization results, case W-III is MADS's optimized in conjunction with the FSP and $EFIC$ formulations. As shown in Fig. 21, $EFIC$ has no significant effect on MADS, but FSP has reduced the objective value to 1,059 W, which is about 9% less than that obtained by $EFIC$. This reduction is, however, at the cost of converging to a larger constraint violation, resulting in a temperature profile that is less corresponding to the target value, which is 276 K (Fig. 22). This causes the runback ice to occur within the protected zone on the upper surface.

5.2 Evaporative regime

In the evaporative regime, not only the protected zone is kept free of ice, but also no runback ice formation is allowed. More constraints are then required to control the ice accretion over the surface. The following three constraints are considered as the first case, Case E-I:

$$\begin{aligned} c_1(\mathbf{x}) &\equiv MIG, \\ c_2(\mathbf{x}) &\equiv EFH, \\ c_3(\mathbf{x}) &\equiv MST. \end{aligned} \tag{18}$$

The above combination of the constraints implies that ice shall not accrete within the protected zone and that the water film shall not pass beyond the zone. Moreover, since higher values of temperature are required in the evaporative regime, a third constraint is imposed to ensure that the temperature of the composite shell does not exceed T_*, which is assumed to be 345 K (Capey 1965). The history of the best feasible objective values is shown in Fig. 23 and the optimized and experimental power densities are compared in Fig. 24. The optimized total electric power is 2,782 W, which is remarkably 35% less than the value used in the experimental test (Run #91, TTMS #122), i.e. 4,269 W (Al-Khalil et al. 1997). This significant reduction in the power usage not only saves the energy but also avoids high temperature values inside the composite shell. Fig. 25 shows that the maximum temperature value inside the composite shell for the optimized state is $337\,K$, which is $95\,K$ less than the maximum experimental value, i.e. $432\,K$. The temperature contour plots also suggest that it is more efficient to push back the intense power density on the upper surface to the end of the protected zone.

Similar to the running-wet regime, MIG can be replaced by MWT, with the same $T_0 = 276\,K$:

$$\begin{aligned} c_1(\mathbf{x}) &\equiv MWT, \\ c_2(\mathbf{x}) &\equiv EFH, \\ c_3(\mathbf{x}) &\equiv MST. \end{aligned} \tag{19}$$

Fig. 26 shows that the optimized total electric power is 2,987 W, which is 7% larger than that obtained in Case E-I, i.e. 2,782 W, because of the margin taken above the freezing temperature. Comparing the power increase of Case E-II with respect to Case E-I (7%) with that of Case W-II with respect to Case W-I (32%), we can conclude that respecting a specific margin in the running-wet regime is more expensive than that in the evaporative regime.

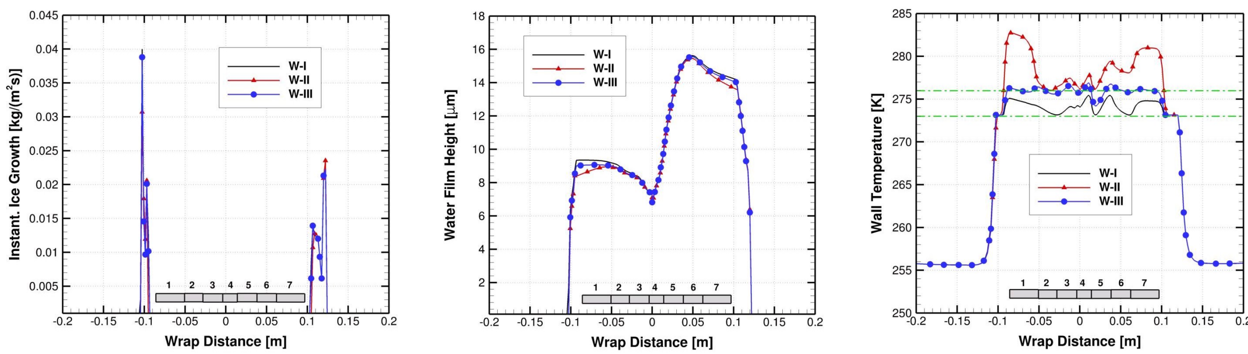

Figure 20: Profiles of three surface quantities for various cases at optimal states

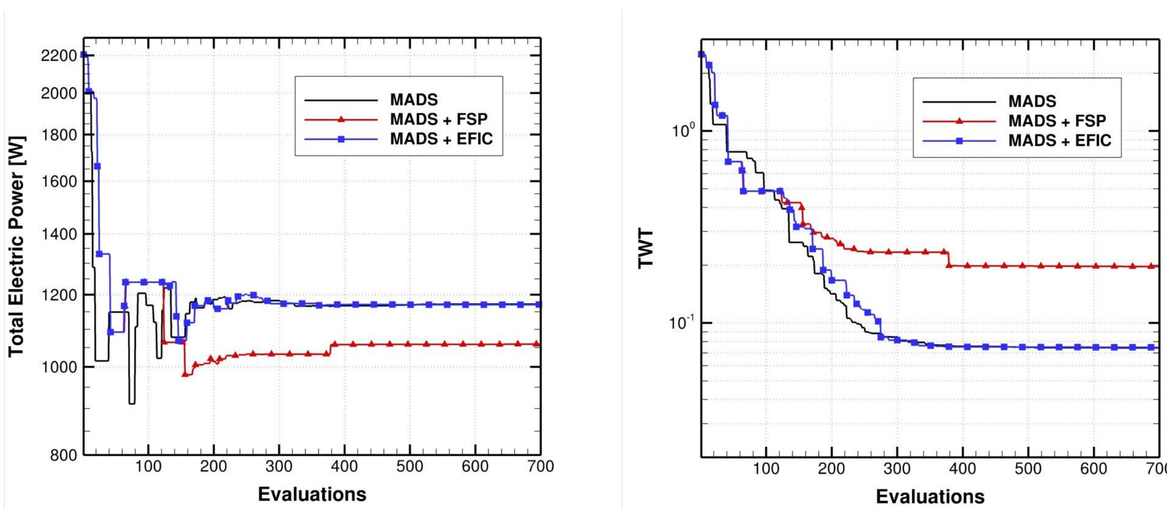

Figure 21: History of the objective values (left) based on the best constraint violation values (right) by different methods (Case W-III)

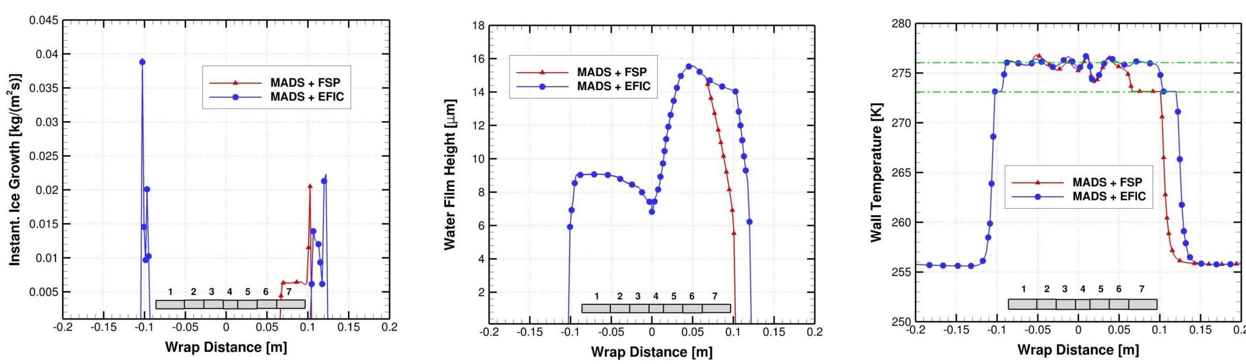

Figure 22: Profiles of three surface quantities for various methods at optimal states (Case W-III)

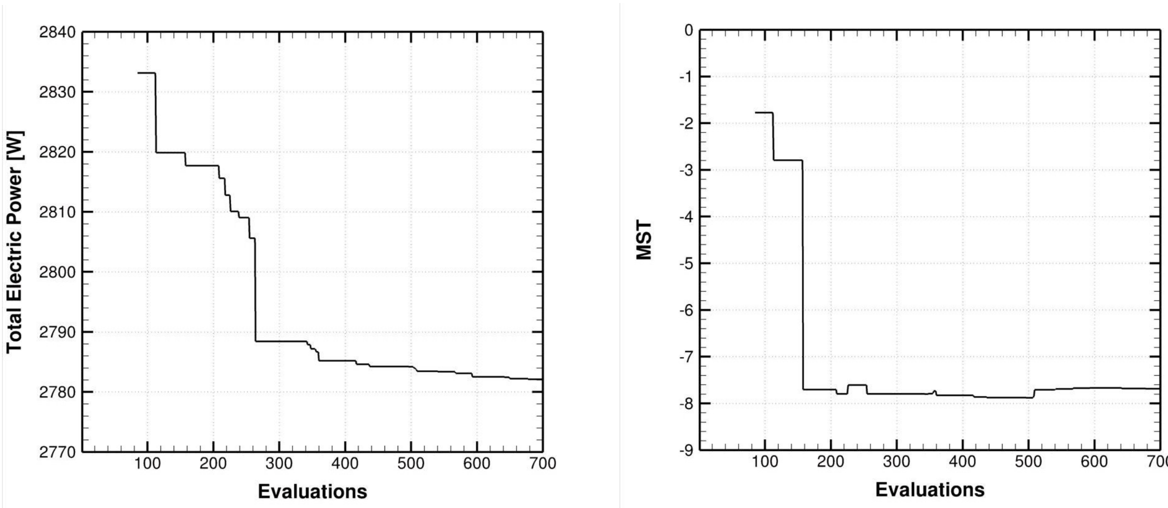

Figure 23: History of the best feasible objective (left) and constraint violation (right) values (Case E-I)

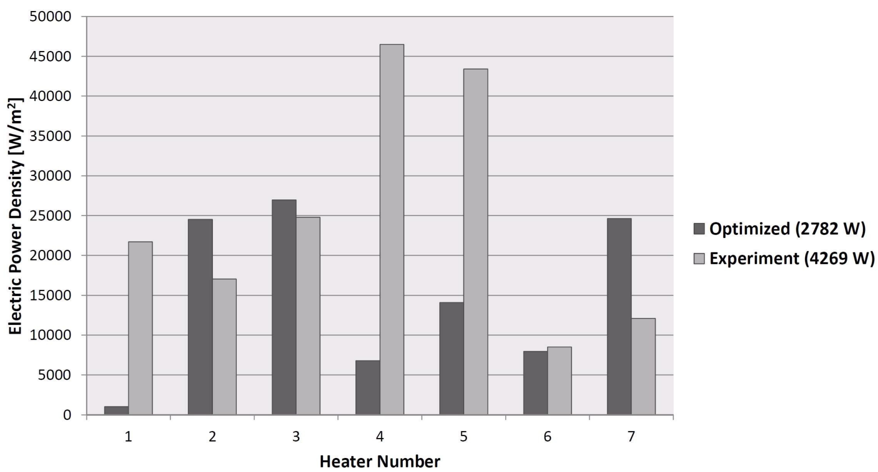

Figure 24: Optimized and experimental power densities (Case E-I)

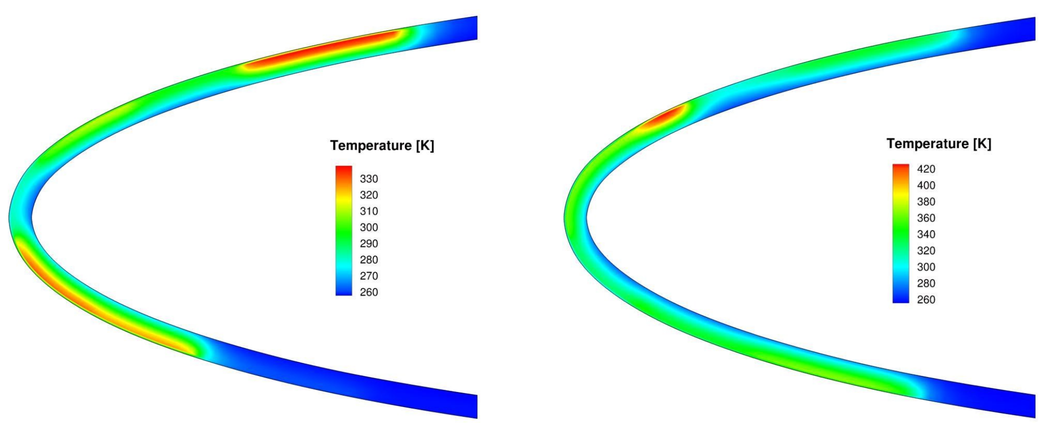

Figure 25: Optimized (left) and experimental (right) temperature contour plots inside the solid shell (Case E-I)

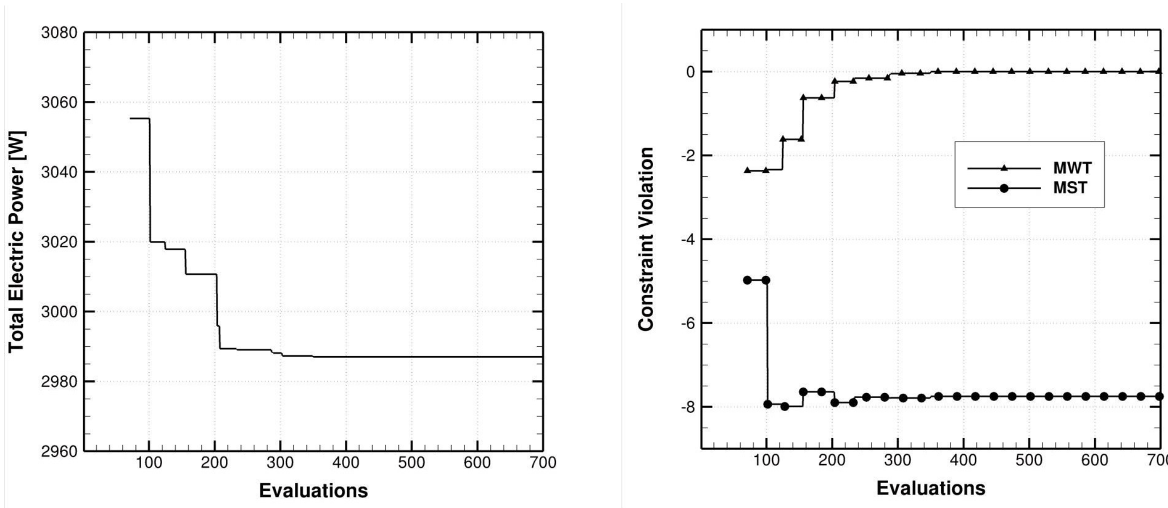

Figure 26: History of the best feasible objective (left) and constraint violation (right) values (Case E-II)

In the evaporative regime, it would be meaningless to use TWT because it is in contradiction to EFH. Instead, the following sets of the constraints are used in cases E-III and E-IV, respectively:

$$\begin{aligned} c_1(\mathbf{x}) &\equiv (TMWT)_d\,, \\ c_2(\mathbf{x}) &\equiv EFH, \\ c_3(\mathbf{x}) &\equiv MST. \end{aligned} \tag{20}$$

$$\begin{aligned} c_1(\mathbf{x}) &\equiv (TMWT)_c\,, \\ c_2(\mathbf{x}) &\equiv EFH, \\ c_3(\mathbf{x}) &\equiv MST. \end{aligned} \tag{21}$$

Fig. 27 compares the history of the best feasible objective function values for Cases E-II, E-III and E-IV. It shows that Case E-II has the best performance in terms of convergence rate and final optimized value. Fig. 28 shows that the optimized power densities for the three cases are closely similar except for heaters 5 and 7 in Case E-IV. The profiles of two surface quantities at their optimal states are compared among the different cases in Fig. 29 (In the evaporative regime, there is no ice accretion on the surface, and thus the ice growth profiles are not plotted). In all cases, the complete evaporation of water film takes place prior to the end of the heating zone. Also as expected, the surface temperature profiles show that Case E-I is not reliable enough as the minimum temperature is very close to the freezing point.

Each of the Cases E-II to E-IV, may be restated using $DEFH$ as the following four-constraint sets for Cases E-V to E-VII, respectively:

$$\begin{aligned} c_1(\mathbf{x}) &\equiv MWT, \\ c_2(\mathbf{x}) &\equiv (DEFH)_{up}\,, \\ c_3(\mathbf{x}) &\equiv (DEFH)_{lo}\,, \\ c_4(\mathbf{x}) &\equiv MST. \end{aligned} \tag{22}$$

$$\begin{aligned} c_1(\mathbf{x}) &= (TMWT)_d\,, \\ c_2(\mathbf{x}) &= (DEFH)_{up}\,, \\ c_3(\mathbf{x}) &= (DEFH)_{lo}\,, \\ c_4(\mathbf{x}) &= MST. \end{aligned} \tag{23}$$

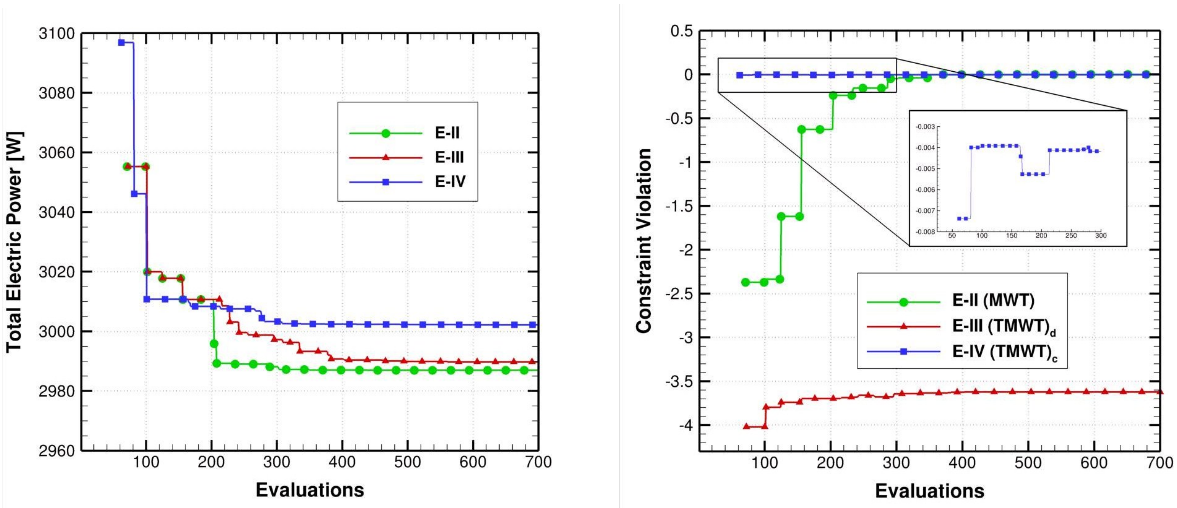

Figure 27: History of the best feasible objective (left) and constraint violation (right) values for different cases

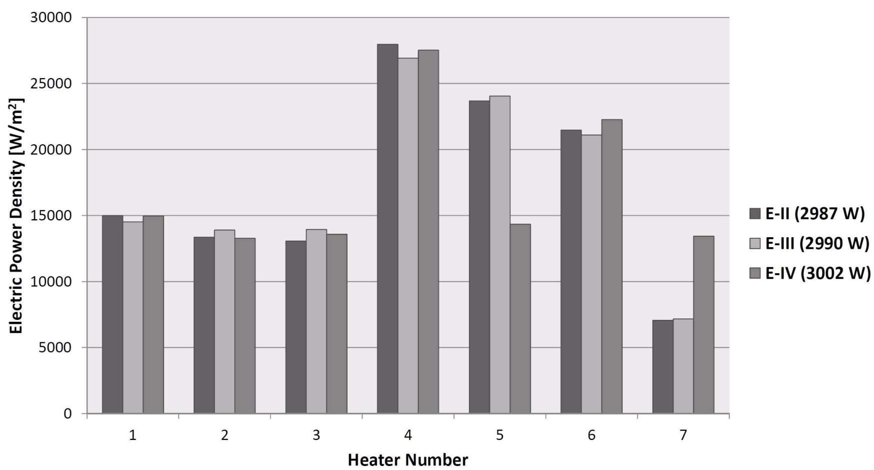

Figure 28: Optimized power densities for different cases

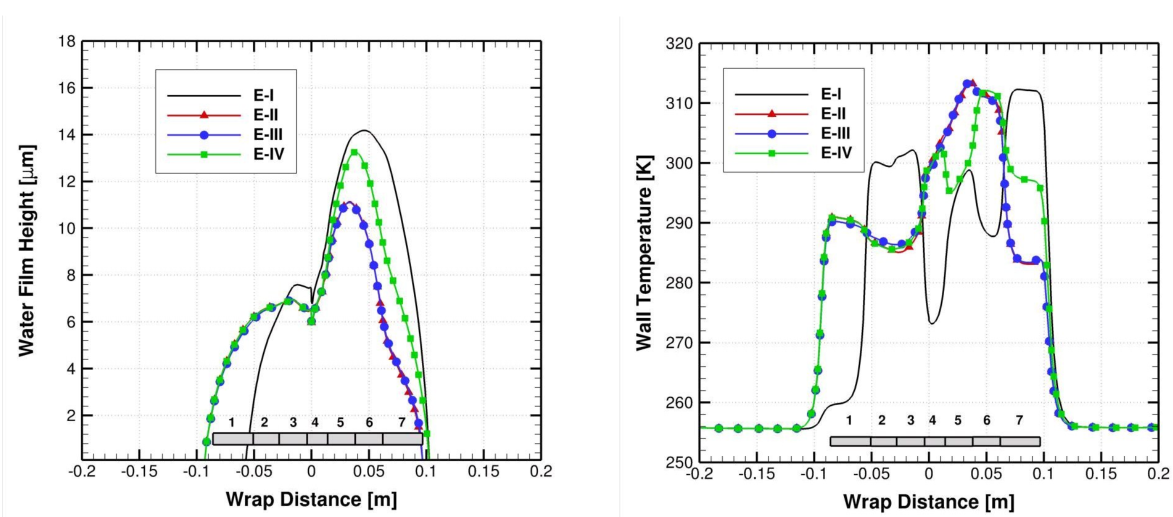

Figure 29: Profiles of two surface quantities for various cases at optimal states

$$
\begin{aligned}
c_1(\mathbf{x}) &= (TMWT)_c\,,\\
c_2(\mathbf{x}) &= (DEFH)_{up}\,,\\
c_3(\mathbf{x}) &= (DEFH)_{lo}\,,\\
c_4(\mathbf{x}) &= MST.
\end{aligned}
\tag{24}
$$

The history of the best feasible objective function values for Cases E-V, E-VI and E-VII is shown in Fig. 30. The superior performance of Case E-VI, which uses $(TMWT)_d$, is clearly seen in terms of both convergence rate and final optimized value. Fig. 31 shows the optimized power densities for the three cases. To compare the influence of EFH and $DEFH$, the convergence history for Cases E-II to E-VII is illustrated in Fig. 32. It shows that each $DEFH$ case has a better performance, i.e. lower total power electric, compared to its equivalent EFH case. It also reveals that Case VI has the best performance among all test cases. A feature of Case VI that was found to be distinct from the other cases is that the maximum composite shell temperature in this case is almost equal to the boundary value, i.e. 345 K, while in all other cases, the maximum temperature varied between 335 K and 338 K (Fig. 32).

The evaporative test cases presented so far has been optimized using MADS without statistical surrogates. To demonstrate the influence of these surrogates on the optimal results, Case E-VI is optimized by MADS

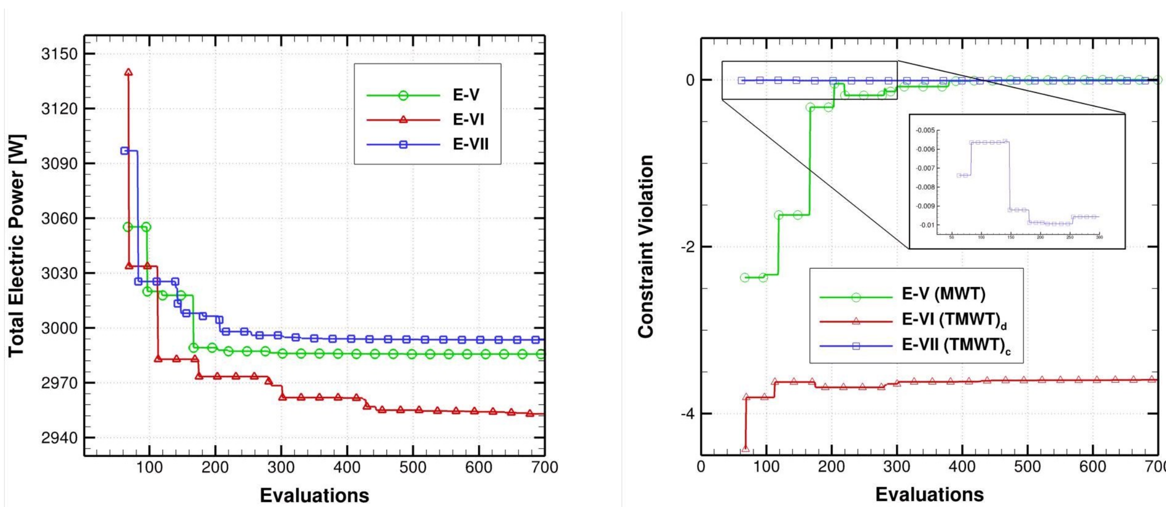

Figure 30: History of the best feasible objective (left) and constraint violation (right) values for different cases

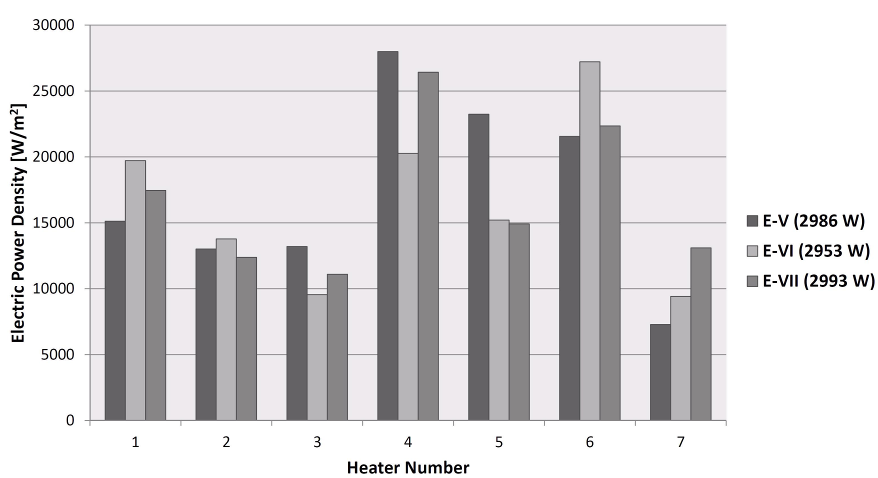

Figure 31: Optimized power densities for different cases

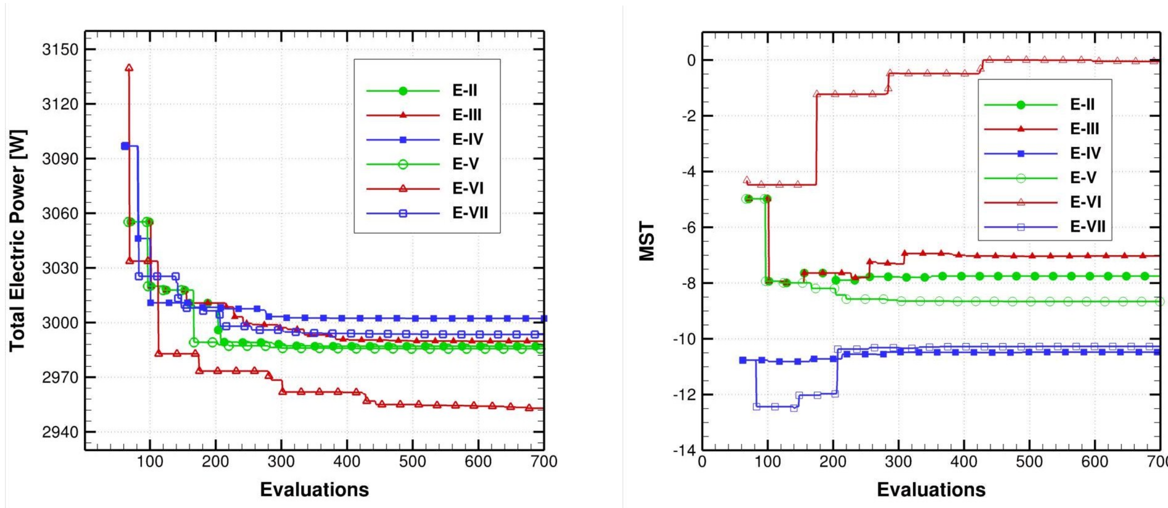

Figure 32: History of the best feasible objective (left) and constraint violation (right) values for different cases

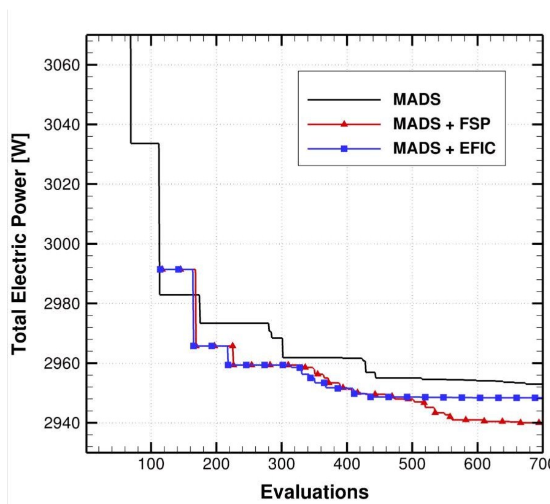

Figure 33: History of the best feasible objective values by different methods (Case VI)

in conjunction with FSP and $EFIC$ models. Fig. 33 shows that these two models have almost the same convergence rate up to the 500th evaluation, after which FSP makes a progressive reduction. The figure also shows that both models have improved the convergence rate as well as the final optimized value compared to MADS without any statistical surrogates.

6 Conclusions

This work presented a set of suitable constraint formulations for the power optimization of an electro-thermal anti-icing system in both running-wet and evaporative regimes. It was demonstrated that for the running-wet regime, the best result is obtained when a proper target temperature is set as the constraint. For the evaporative regime, the best result is obtained when using a quantifiable constraint, i.e. one that provides a distance to infeasibility as well as a distance to feasibility. The physical and mathematical logics behind the proposed formulations may also be useful to other engineering optimization problems. The optimal solutions were also compared against experimental data, which showed a significant reduction in the power requirement by the optimal results.

The influence of using two different statistical relevance criteria on the performance of the optimization method, i.e. the Mesh Adaptive Direct Search (MADS) algorithm, was investigated. It was shown that, especially for the evaporative test cases, a criterion based on a chance constraint performs better than the one based on the expected feasibility improvement.

Future work may consist of investigating the effect of the thickness and type of different materials inside the composite shell in order to improve the heat transfer through the shell. Optimization of the electro-thermal system in deicing mode is another potential research area.

References

Al-Khalil K, Horvath C, Miller D, Wright W (1997) Validation of thermal ice protection computer codes: part 3-the validation of ANTICE. Paper presented at the 35th Aerospace Sciences Meeting and Exhibit, AIAA Paper 97–0051, Reno, NV, USA, January 1997

Audet C, Béchard V, Le Digabel S (2008) Nonsmooth optimization through mesh adaptive direct search and variable neighborhood search. Journal of Global Optimization 41(2):299–318

Audet C, Dennis J (2006) Mesh adaptive direct search algorithms for constrained optimization SIAM Journal on Optimization 17(1):188–217

Baker AA, Dutton S, Kelly DW (2004) Composite materials for aircraft structures. Second edn. AIAA, Reston, Virginia, USA

Beaugendre H, Morency F, Habashi WG (2006) Development of a second generation in-flight icing simulation code. Journal of Fluids Engineering 128(2):378–387 doi:10.1115/1.2169807

Buschhorn ST, Lachman N, Gavin J, Wardle BL, Kessler SS, Thomas G (2013) Electrothermal icing protection of aerosurfaces using conductive polymer nanocomposites. Paper presented at the 54th AIAA/ASME/ASCE/AHS/ASC Structures, Structural Dynamics, and Materials Conference, AIAA Paper 1729–2013, Boston, Massachusetts, USA, April 2013

Capey EC (1965) Alleviation of thermal stresses in aircraft structures. Aeronatical Research Council, London, UK

Clarke FH (1983) Optimization and nonsmooth analysis. John Wiley & Sons, New York, USA

Croce G, Beaugendre H, Habashi WG (2002) CHT3D: FENSAP-ICE conjugate heat transfer computations with droplet impingement and runback effects. Paper presented at the 40th Aerospace Sciences Meeting and Exhibit, AIAA Paper 2002-0386, Reno, NV, USA, January 2002

da Silva GAL, Silvares OM, Zerbini EJGJ (2005) Simulation of an airfoil electro-thermal anti-ice system operating in running wet regime. Paper presented at the 43rd AIAA Aerospace Sciences Meeting and Exhibit, AIAA Paper 2005–1374, Reno, NV, USA, January 2005

Dussin D, Fossati M, Guardone A, Vigevano L (2009) Hybrid grid generation for two-dimensional high-Reynolds flows. Computers & Fluids 38(10):1863–1875

Goldberg DE (1989) Genetic algorithms in search, optimization, and machine learning. vol 412. Addison-Wesley, Menlo Park, California, USA

Gramacy RB, Taddy MA (2010) dynaTree: An R package implementing dynamic trees for learning and design.

Hackerman N (1952) Effect of temperature on corrosion of metals by water. Industrial & Engineering Chemistry 44(8):1752–1755

Jones DR (2001) A taxonomy of global optimization methods based on response surfaces. Journal of Global Optimization 21(4):345–383

Jones DR, Schonlau M, Welch WJ (1998) Efficient global optimization of expensive black-box functions. Journal of Global Optimization 13(4):455–492

Le Digabel S (2011) Algorithm 909: NOMAD: Nonlinear optimization with the MADS algorithm. ACM Transactions on Mathematical Software 37(4):44:41–44:15

Mayer C, Ilinca A, Fortin G, Perron J (2007) Wind tunnel study of electro-thermal de-icing of wind turbine blades. International Journal of Offshore and Polar Engineering 17(3):182

McKay MD, Beckman RJ, Conover WJ (2000) A comparison of three methods for selecting values of input variables in the analysis of output from a computer code. Technometrics 42(1):55–61

Messinger BL (1953) Equilibrium temperature of an unheated icing surface as a function of air speed. Journal of the Aeronautical Sciences 20(1):29–41

Miller D, Bond T, D S, Wright W, Langhals T, Al-Khalil K, Broughton H (1997) Validation of thermal ice protection computer codes: part 1-program overview. Paper presented at the 35th AIAA Aerospace Sciences Meeting and Exhibit, AIAA Paper 97–0049, Reno, NV, USA, January 1997

Mivehchi H, Varvani-Farahani A (2010) The effect of temperature on fatigue strength and cumulative fatigue damage of FRP composites. Procedia Engineering 2(1):2011–2020

Pourbagian M, Habashi WG (2012) Parametric analysis of energy requirements of in-flight ice protection systems. Paper presented at the 20th Annual Conference of the CFD Society of Canada, Canmore, Alberta, Canada, May 2012

Pourbagian M, Habashi WG (2013a) CFD-based optimization of electro-thermal wing ice protection systems in de-icing mode. Paper presented at the 51st AIAA Aerospace Sciences Meeting including the New Horizons Forum and Aerospace Exposition, AIAA Paper 2013–0654, Grapevinve, Texas, USA, January 2013

Pourbagian M, Habashi WG (2013b) On optimal design of electrothermal in-flight ice protection systems. Paper presented at the 5th AIAA Atmospheric and Space Environments Conference AIAA Paper 2013–2937, San Diego, California, USA, June 2013

Pourbagian M, Habashi WG (2013c) Surrogate-based optimization of electrothermal wing anti-icing systems. Journal of Aircraft 50(5):1555–1563 doi:10.2514/1.C032072

Reid T, Baruzzi GS, Ozcer I, Habashi WG (2011) FENSAP-ICE: 3D simulation, and validation, of d-icing with inter-cycle ice accretion. Paper presented at the SAE 2011 International Conference on Aircraft and Engine Icing and Ground Deicing, SAE Paper 2011–38–0102, Chicago, USA, June 2011

Reid T, Baruzzi GS, Ozcer I, Switchenko D, Habashi WG (2013a) FENSAP-ICE simulation of icing on wind turbine blades, part 1: performance degradation. Paper presented at the 51st AIAA Aerospace Sciences Meeting including the New Horizons Forum and Aerospace Exposition, AIAA Paper 2013–0750, Grapevine, Texas, US, January 2013

Reid T, Baruzzi GS, Ozcer I, Switchenko D, Habashi WG (2013b) FENSAP-ICE simulation of icing on wind turbine blades, part 2: ice protection system design. Paper presented at the 51st AIAA Aerospace Sciences Meeting including the New Horizons Forum and Aerospace Exposition, AIAA Paper 2013–0751, Grapevine, Texas, USA, January 2013

Schonlau M, Welch WJ, Jones DR (1997) Global versus local search in constrained optimization of computer models. Paper presented at the 1997 Joint AMS-IMS-SIAM Summer Conference, Washington, Seattle, USA, July 1997

Sinnett M (2007) 787 No-bleed systems: saving fuel and enhancing operational efficiencies. Boeing Commercial AERO magazine 4(1):6–11

Starke EAJ (1996) Accelerated aging of materials and structures, the effects of long-term elevated-temperature exposure. National Academy Press, Washington D.C., USA

Strehlow RH, Moser R (2009) Capitalizing on the increased flexibility that comes from high power density electrothermal deicing. Flight Dynamics 2000:03–01

Taddy MA, Gramacy RB, Polson NG (2011) Dynamic trees for learning and design. Journal of the American Statistical Association 106(493):109-123

Talgorn B, Le Digabel S, Kokkolaras M (2014) Problem formulations for simulation-based design optimization using statistical surrogates and direct search. Technical Report, Les Cahiers du GERAD G–2014–04, HEC Montréal, Canada

Thomas SK, Cassoni RP, MacArthur CD (1996) Aircraft anti-icing and de-icing techniques and modeling. Journal of Aircraft 33(5):841–854

Vaz AIF, Vicente LN (2007) A particle swarm pattern search method for bound constrained global optimization. Journal of Global Optimization 39(2):197–219

Wright W, Al-Khalil K, Miller D (1997) Validation of NASA thermal ice protection computer codes: part 2-the validation of LEWICE/Thermal. Paper presented at the 35th AIAA Aerospace Sciences Meeting and Exhibit, AIAA Paper 97–0050, Reno, NV, USA, January 1997

Yaslik AD (1991) Three-dimensional numerical simulation of transient heat transfer occurring in electrothermal deicing systems. PhD Thesis, University of Toledo